Title

Structural stability of mechanically alloyed amorphous (FeCoNi)70Ti10B20 under high-temperature and high-pressure

Authors

Avar, Baris
Simsek, Tuncay
Ozcan, Sadan
et al.

Publication Date

2021-04-01

DOI

10.1016/j.jallcom.2020.158528

Peer reviewed

Structural stability of mechanically alloyed amorphous $(FeCoNi)_{70}Ti_{10}B_{20}$ under high-temperature and high-pressure

Baris AVAR[1*], Tuncay SIMSEK[2], Sadan OZCAN[3], Arun K. CHATTOPADHYAY[4], Bora KALKAN[5,6]

[1]Department of Metallurgical and Materials Engineering, Zonguldak Bülent Ecevit University, Zonguldak, 67100, Turkey

[2]Department of Mechanical and Metal Technologies, Kırıkkale University, Kırıkkale, 71450, Turkey

[3]Department of Physics Engineering, Hacettepe University, Ankara, 06800, Turkey

[4]Uniformity Labs, 41400 Christy Street, Fremont, CA, 94538, USA

[5]Advanced Light Source, Lawrence Berkeley National Laboratory, Berkeley, CA, 94720, USA

[6]Earth and Planetary Sciences Department, University of California, Santa Cruz, CA, 95064, USA

[*]Corresponding author. Tel.:+90 372 291 2595; E-mail address: barisavar@beun.edu.tr

Abstract

Nanostructured $(FeCoNi)_{70}Ti_{10}B_{20}$ (at%) alloy was synthesized by mechanical alloying from elemental powder mixture of Fe, Co, Ni, Ti and B using ball milling. The effect of ball milling time on the evolution of structure and morphology was investigated by X-ray diffraction, scanning and transmission electron microscopy and differential thermal analysis. It was observed that the formation of solid solution of $(FeCoNi)_{70}Ti_{10}B_{20}$ started from the very onset of the milling process. Crystallite size and lattice strains seemed to be leveled off after 20 hours of milling with no further major changes. The milling process for longer periods introduced severe plastic deformations causing formation of amorphous phase of $(FeCoNi)_{70}Ti_{10}B_{20}$. The amorphous alloy composition was confirmed by energy dispersive X-ray spectroscopy analysis that showed an excellent homogeneity of the alloying elements. The phase stability of the mechanically alloyed amorphous sample was further verified by employing high-temperature and high-pressure studies. The alloy samples heat-treated at 700 °C revealed crystallization of the amorphous phase. However, synchrotron-based high-

pressure ambient temperature X-ray diffraction studies confirmed that the amorphous phase of the alloy remained stable up to the pressure of 30 GPa. The 50 h milled sample after being annealed at 350 °C showed improvement in the soft magnetic properties of the alloy, which was due to the probable elimination of the residual stress in the amorphous phase of the alloy powders.

Keywords: Mechanical alloying; Amorphous; High-pressure; Alloy; Soft magnetic behavior

1. Introduction

With the growth of newer technologies, the demand for soft magnetic materials has been on the rise rapidly. Pure iron is a good ferromagnetic material with a low resistivity, and it leads to a large eddy current loss in high frequency electronic devices (GHz). When it is alloyed, higher magnetic permeability and lower total losses can be achieved ascertaining higher device efficiency [1,2]. The observed enhancement in permeability and electrical resistivity through the inclusion of nickel into the iron lattice motivated material researchers to discover a variety of Fe-based amorphous-nanocrystalline alloys [3,4]. Furthermore, the addition of cobalt in Fe-based amorphous-nanocrystalline alloys is known to increase Curie temperature and forms HITPERM alloys suitable for designing materials for high temperature applications [5]. In view of that, several different amorphous/nanocrystalline magnetic materials have been developed by combination of late transition metals (Fe, Co, Ni), early transition metals (Ti, Zr, Nb, etc.) and metalloids (B, P, Si, etc.) [5,6].

These alloys can be synthesized by various methods. However, mechanical alloying (MA) happens to be the most common and preferred one due to its simplicity, and it is relatively a low-cost process with good control on synthesis parameters. It also has good ability to produce alloys via equilibrium and non-equilibrium states of materials at room temperature

either from their elemental or compounded powder forms. The powder blends and milling media (metal or ceramic balls) are kept in a hard vial and severe plastic deformations are imposed on the powders during milling. As a result, alloying materials are subjected to stress, fracture, and cold welding that result into the formation of supersaturated solid solutions, from which nanocrystalline, quasicrystalline and amorphous structures are shaped. The microstructure and particle size of the synthesized powders can be controlled by optimizing synthesis parameters such as ball-to powder ratio, rotating speed, process control agent, duration of synthesis etc. [7,8]. It is well known that the soft magnetic properties can be enhanced by altering the microstructure and reducing the crystallite size to nanoscale. As per the random anisotropy model, the enhancement of soft magnetic properties in nanomaterials can occur due to the averaging effect of magnetocrytalline anisotropy when the particle size becomes smaller than the magnetic exchange length [9,10].

Due to the observed benefits from MA method for the processing of magnetic materials, during past few years multiple studies were carried out on Fe-TM-B (TM = transition metal) based amorphous/nanocrystalline alloys [11–15]. Simsek et al. [11] reported that during MA of $Fe_{70}Ti_{10}B_{20}$ (at.%) powders, the Fe(TiB) solid-solution was obtained in the beginning of the milling, followed by the amorphous phase formation. Raanaei et al. studied the mechanically alloyed $Co_{49}Ni_{21}Ti_{10}B_{20}$ [12], and $Fe_{49}Co_{21}Mn_{10}Ti_{10}B_{10}$ powders [13], while Abbasi et al. [14] investigated the mechanically alloyed $Fe_{47}Ni_{23}Ti_{10}B_{20}$ powders. These reports described the formation of nanocrystalline and amorphous alloy structures by increasing the milling time. In another study Du and Ramujan delineated three different nanocrystalline compositions viz. $Fe_{40}Ni_{38}B_{18}Mo_4$, $Fe_{49}Ni_{46}Mo_5$ and $Fe_{42}Ni_{40}B_{18,}$ produced by MA, where all three alloy compositions were in the form of fcc-solid solution of the alloying components. The presence of Mo seemed to have affected the characteristics of the alloy phases. For example, in the absence of Mo, Fe_3B phase was formed in the $Fe_{42}Ni_{40}B_{18}$ alloy, whereas the presence Mo in

$Fe_{40}Ni_{38}B_{18}Mo_4$ alloy prevented the formation of any iron boride phase [15]. Unfortunately, the phase stability of these alloys under various thermodynamic conditions are not very well understood, particularly under high-temperature and high-pressure conditions.

The present study aimed at synthesizing a novel $(FeCoNi)_{70}Ti_{10}B_{20}$ (at%) alloy by MA from the elemental powders of Fe, Co, Ni, Ti and B. It was mainly with an intent to develop an alloy of good amorphous-phase stability for superior application as soft-core magnetic material. The structural changes, particle morphology , thermal behavior, magnetic properties and phase stability of the $(FeCoNi)_{70}Ti_{10}B_{20}$ alloy were investigated by X-Ray diffractometry (XRD), scanning electron microscopy with energy dispersive X-ray spectroscopy (SEM/EDX), transmission electron microscopy (TEM), differential thermal analysis (DTA), and vibrating sample magnetometer (VSM). In order to follow the structural changes upon heat treatment, the alloyed powders were studied and analyzed by XRD. Phase stability of synthesized samples were also examined under high pressure (0-30 GPa) using synchrotron radiation XRD.

2. Experimental Procedure

2.1. Sample preparation

Elemental powders of Fe (Aldrich, 99.9%), Co (Aldrich, 99.9%), Ni (Aldrich, 99.9%), Ti (Aldrich, 99.9%) and B (Aldrich, 99.9%) were used as starting materials. To ascertain the nominal alloy composition of the alloy as 23.33 at.% Fe, 23.33 at.% Co, 23.33 at.% Ni, 10 at.% Ti, 20 at.% B, the elemental powders were weighed accordingly and blended in an argon filled glovebox. Mechanical alloying of the elemental powder mix was carried out in a planetary type ball mill (Retsch-PM100 CM) at room temperature. The hardened steel balls and hardened steel vial were used for milling conducted under argon atmosphere. The ball-to-powder ratio was kept at 20:1 and milling speed was adjusted to 500 rpm, as the same as

previous experiments [11,16]. The mill rotational direction was reversed at a steady interval in order to avoid excessive heat building and to prevent powders from sticking to the walls and balls. For avoiding contamination, powders were ball milled without using any process control agent (PCA). Sampling of the milled powder for characterization was conducted in an argon filled glovebox in order to prevent any unwarranted oxidation.

2.2. Characterization

The morphological and microstructural properties of the milled $(FeCoNi)_{70}Ti_{10}B_{20}$ (at%) powders were analyzed using scanning electron microscope (SEM) equipped with energy dispersive X-ray spectroscopy (EDX) (FEI Quanta FEG 450) at 14 kV in secondary electron imaging mode, and high-resolution transmission electron microscopy (HRTEM, Jeol 2100F). The mean particle and grain size distributions of milled powder samples collected at preselected periods were estimated by ImageJ software [17]. The phase identification and structural evolutions were followed by X-ray diffraction (XRD) (Panalytical Empyrean) with Cu-Kα radiation produced at 45 kV and 40 mA, between 20° and 80° diffraction angles (2θ) in 0.013° step size. The crystallite size and the lattice strain of the samples were estimated using single peak analysis program of X'pert High Score Plus software through the pseudo-voigt function analysis [18]. Thermal stability of the milled powders was analyzed by differential thermal analysis (DTA) using a SII Exstar TG/DTA 7200. The samples were heated in alumina crucibles from 200 to 1150 °C at a heating rate of 20 °C/min under 40 ml min^{-1} nitrogen flow. The heat-treatment process was also performed in the DTA equipment with a heating rate of 20 °C/min.

The 50 h milled sample was used for studying phase stability of the synthesized alloy powder. High-pressure XRD data were obtained using samples in a gasketed diamond anvil cell (DAC) mounted on the synchrotron X-ray beam. High-pressure was applied to the sample at an ambient temperature using a standard symmetric diamond anvil cell (DAC) with 300 μm

culet diamonds and c-BN (boron nitride) backing plates on the synchrotron and detector sides. Samples were contained within Rhenium gaskets. Rhenium gaskets were indented to a thickness of about 50 μm. For diffraction measurements, a 140-μm hole was drilled in the center of the indentation and was loaded with the sample, with 4:1 methanol-ethanol mixture as the quasi-hydrostatic pressure-transmitting fluid, and small spheres of ruby as pressure markers to estimate pressures by ruby fluorescence method. High pressure and ambient pressure X-ray diffraction data were collected at room temperature on beamline 12.2.2 of the Advanced Light Source. The X-ray energy used was 30 keV (0.4133 Å) and refined sample-to-detector distance was 330 mm. X-ray diffraction images were collected using a mar345 image plate detector, and processed using the Dioptas software package [19]. The magnetic characterizations were carried out by using a vibrating sample magnetometer (VSM) (Lake Shore 7407) at 23 °C within ± 20 kOe magnetic field range.

3. Results and Discussions

3.1. Structural changes

XRD pattern of starting mixture is shown in Figure 1. The characteristic crystalline peaks for the phases of Fe (ICDD Card No:87-0721, cubic, *Im-3m*), Co (ICDD Card No:05-0727, hexagonal, *$P6_3/mmc$*), Ni (ICDD Card No:04-850, cubic, *Fm-3m*) and Ti (ICDD Card No:44-1294, hexagonal, *$P6_3/mmc$*) are clearly identified. However, the peaks of boron could not be identified due to its low atomic scattering factor.

The XRD patterns of the $(FeCoNi)_{70}Ti_{10}B_{20}$ (at%) collected at preselected milling periods (1 h-50 h) are shown in Figure 2a. As one can follow from the XRD patterns, the peaks of all Fe, Co, Ni and Ti phases of 1 h milled sample were substantially marginalized and excepting Fe, they almost disappeared after 3 h of milling. With the continuation of milling, the diffraction Bragg peaks of Fe (110) became broadened with diminished intensity. This is mainly due to

the reduction in crystallite size and increase in the lattice strain. By prolonging milling time, the Brag peak at around 44.65^{o} continued to broaden with slight shift towards lower angles which can be attributed to the formation of solid solution of $(FeCoNi)_{70}Ti_{10}B_{20}$ phase. A similar behavior was also observed by Wederni et al. in nanostructured $Fe_{60}Al_{35}Sn_5$ synthesized by MA of Fe, Al and Sn powders [20]. After ~20h of milling, the powders appear to constitute a dominant amorphous solid solution. The relative amorphous phase fractions estimated from the integrated peak areas of the relevant diffraction peaks as a function of the milling time is shown in Figure 2b [21]. The rapid amorphization of $(FeCoNi)_{70}Ti_{10}B_{20}$ alloy was observed in the very beginning of milling because of lattice destabilization of very high order. Lattice destabilization occurs due to the huge strain energy stored in the alloying mass during continuous deformation as the milling progresses. Schwarz et al. also reported solid-state amorphization through interdiffusion of the alloying elements, for which, large thermodynamic driving force was necessary to drive the elements for interdiffusion generating large negative heat of mixing during milling [22]. However, to produce amorphous alloys, there are three empirical rules suggested by Inoue [23] as follows: (i) multicomponent alloy systems with three or more elements; (ii) a significant difference in atomic radius ratios above ~12% among the main constituent elements; and (iii) a large negative heat of mixing (ΔH_{mix}) among the alloying elements. The present alloy system consists of five elements, and three of them has equal concentration as the main host components. According to the Table 1, main host components (Fe,Co,Ni) have negative heats of mixing against Ti, and B. Also, the atomic size ratios for Fe, Co and Ni with Ti and B are larger than 12 %. All these factors enable to reduce the diffusivity and retard the rearrangement of the atoms of constituent elements on a long-range scale [23,26]. Thus, amorphous phase formation in the mechanically alloyed $(FeCoNi)_{70}Ti_{10}B_{20}$ powders is possible in thermodynamic viewpoint. As it is seen in Figure 2b, the amorphization was very fast during the first 10 h of milling. After 50h of

milling nearly all crystal phases were disappeared and XRD revealed fully amorphized phases of $(FeCoNi)_{70}Ti_{10}B_{20}$. These results suggest a phase transformation sequence following the path expressed below in Equation 1.

Fe + Co + Ni + Ti + B ⟶ α-Fe solid solution phase ⟶ Amorphous phase (1)

The crystallite size and lattice strain of the mechanically alloyed powders as a function of the milling time are given in Figure 3a. A sharp decrease in crystallite size was observed during the first 5 h of milling due to the comminution of starting elemental powders, which continued further to be diminished to reach a size of 2.2 ± 1 nm after 20 h of milling. The decrease in crystallite size is mostly attributed to the simultaneous effects of milling-induced plastic deformations and dislocations [7]. Dislocations cause crystallographic defects and irregularities within a crystal structure due to the sudden changes in the arrangement of atoms. During milling the stress induced plastic deformation of the alloying elements promotes internal micro-deformation and mechanical distortion that creates many dislocations of atoms in the crystal lattice causing lattice strains to increase. The longer the milling time, the higher the dislocations and the higher the lattice strains (Figure 3a). The lattice strain was calculated as 0.56 % at 1 h and it increased to 4.296 % after 20 h of milling. The changes in lattice parameter with milling time are shown in Figure 3b, and showing good agreement with the results obtained from Fe(Al,Sn) solid solution powder [20]. The decrease of the lattice parameters during 1 h of milling is probably due to the compressive forces caused by collisions [27,28]. Then, from 1 h to 20 h of milling, lattice parameters increase which can be attributed to the severe plastic deformations, formation of large number of structural defects such as stacking faults, grain boundaries, and enhanced dislocations density (Figure 3c) during the milling process resulting in amorphization [29]. The severe plastic deformations are originated from the impacts between the particles, milling media and the vial. With the progression of milling, the dislocation density of the alloyed powder increases because of

increased grain boundary fraction from the successive accumulation of dislocations owing to fragmentation of crystals to sub-crystallites. Dislocations are of directional nature determined by the distance of movement of the atoms. The distance and direction of movement caused to atoms in the crystal lattice is defined by Burgers vector. The Burgers vector of the dislocation remains constant even though the shape of dislocation may change. One of the principal lattice defects due to dislocation can be determined by the following Equation 2:

$$\rho_D = 2\sqrt{3}\frac{\left(\varepsilon^2\right)^{1/2}}{D.b} \quad (2)$$

where, b refers to the Burgers vectors of dislocation and equals $a\sqrt{3}/2$ for the bcc structure, D is the mean crystallite size and ε is the internal strain. Based on the coherent polycrystal model [30], the volume fraction of the grain boundaries, f_{gb}, was estimated by the formula:

$$f_{gb} = 1 - f_g \quad (3)$$

where f_g denotes the volume fraction of the grains given by

$$f_g = \frac{\left(D-d\right)^3}{D^3} \quad (4)$$

where D is the crystallite size, and d is the effective grain-boundary thickness comprising 2-3 atomic layers, as suggested in ref. [31]. The dislocation density of the alloyed powder calculated by Equation 2 is shown in Figure 3c. The dislocation density of the alloyed powders gradually increased and reached to ~22 x10^{16} m^{-2} at 20 h of milling. The volume fraction of the grain boundary versus milling time is shown in Figure 3d. The increase in volume fraction of grain boundary with milling time as calculated by the Equation 3 and 4 suggested the domination of the amorphous phases with the progression of milling [32].

3.2. Particle morphology and size evolution

The SEM images of particle evolution of the $(FeCoNi)_{70}Ti_{10}B_{20}$ alloys as a function of milling time are given in Figure 4. With increasing milling time, the size of agglomerations was reduced due to continuous re-welding and fracturing. In mechanochemical process the ductile particles get flattened first and welded to each other before they are fragmented. With continuous milling, those mechanisms occur simultaneously initiating deformation hardening of powders. At this stage, the particles are no longer re-welded to each other and remain stable. Further size reduction continues through the simple size reductions by mechanical fragmentation process only. In Figure 4a and 4b, at the very onset of milling, the powders were found to be agglomerated due to the formation of cold welding between the particles. Besides, without using the PCA in the milling process lead to strong agglomeration between the particles that sticking on the walls and the grinding balls [33]. In Figure 4c-e, after 5 h of milling, the morphologies continued to change to spherical one due to mixing of elemental powders, cold welding and homogenization. Size reductions after 20 h of milling, in Figure 4f-h, are mainly from mechanical attrition.

The average particle size distribution of the alloyed powder samples as a function of milling time was determined from SEM images and the average values are shown in Figure 5. In the beginning of the milling (from 1 h to 5 h), average particle size of the powders decreased rapidly to about 77 μm, because of the cracking of the powder particles is caused by the deformation strengthening [7]. With extended milling up to 50 h, the size of the powder particles slightly decreased and reached a minimum value of about 42 μm, corresponds to the completion of the solid-state amorphization reaction, as confirmed by the XRD results in Figure 2a [34].

Figure 6 shows the typical elemental mapping and corresponding EDX analysis of 50 h milled powder sample. It can be seen that Fe, Co, Ni Ti and B were homogenously distributed in $(FeCoNi)_{70}Ti_{10}B_{20}$ alloy. The homogeneous distribution of all alloying element was stimulated from the early equilibrium states reached between cold welding and fracturing of the alloying components. The EDX spectra showed the characteristic peaks of Fe, Co and Ni of the alloy powder and there was no indication of oxygen contamination in the sample.

The morphological structure of 50 h alloyed powders were further analyzed by TEM to get more insights about the microstructures. The bright-field TEM image at both low and high magnifications in Figure 7a shows nanosized grains with an agglomerated morphology. Also, some dark and bright regions were seen in the TEM images. This observed contrast could be attributed to the mass and/or thickness differences of the scanned area of the sample, various orientations of crystal structure or presence of dual-structure [35]. The grain size distribution of the 50 h milled powder particles is shown in Figure 7b. The average grain size of the particles found to be about 3.2 ± 0.52 nm, in agreement with the crystallite size estimated using XRD data. These results indicate that the observed amorphization process in the $(FeCoNi)_{70}Ti_{10}B_{20}$ alloy fulfills the characteristics of the first type (type I) mechanism suggested by Weeber and Bakker [36]. In type I, the amorphization reaction occur due to the continuous reduction of the crystallite size, named as “effective crystallite size”, so the peak broadening signs the amorphous phase formation. In this mechanism, the solid solution phase is considered as the intermediate stage necessary for amorphization [37].

3.3. Thermal analysis and heat-treatments

Figure 8 shows the DTA traces obtained during continuous heating of $(FeCoNi)_{70}Ti_{10}B_{20}$ (at%) powder samples collected at various milling durations. The DTA traces of the 1 h and 3 h milled samples showed no thermal peaks. The DTA traces of alloy samples of 5 h and

beyond displayed two exothermic peaks, a broad one around 400 °C and a distinct one at around 550 °C. However, after 40 h of milling, the broad peak around 400 °C was fully disappeared and the second peak shifted to lower temperatures with reduced intensity. The onset temperature of the exothermic peak (T_x) varied from 520 °C for the 10 h milled sample to 485 °C for the 50 h milled sample. This is because T_x is mainly determined by the chemical composition of materials, as given in Eq.1. During the initial phase, up to 10 h of milling, the exotherm is due to the transformation of the α-Fe solid solution phase into the amorphous phase. As the milling time increases, the T_x shifts towards lower temperature. This observed peak shift can be attributed to the crystallization of the amorphous phase. In order to generate better understanding of such thermal behavior, the 50 h milled sample was further heat-treated in DTA furnace below and above the exothermic peaks observed, at 350 °C and 700 °C, respectively and then the sample was cooled down rapidly to freeze the microstructure for subsequent XRD analysis. Figure 9 shows the XRD patterns of the heat-treated and 50 h milled sample. The XRD of the sample heat-treated at 350 °C revealed no significant difference compared to the original 50 h sample. After heat-treatment at 700 °C, a number of crystalline phases namely; α-Fe (ICDD Card No: 98-018-5728, cubic, Fm-3m), Fe_2O_3 (ICDD Card No: 01-084-0308, rhombohedral, R-3c), $FeNi_3$ (ICDD Card No: 98-063-2929, cubic, Pm-3m), Co_3Ti (ICDD Card No: 98-010-2708, cubic, Pm-3m), TiB_2 (ICDD Card No: 01-075-0967, hexagonal, P6/mmm) were formed in the alloy. Besides, the diffraction pattern from the fully crystalline alloy contains some unidentified reflections. As seen from the Figure 9, the peak positions of the crystalline phases are very close to each other, thus making a distinction between those positions is difficult. It can be concluded that for the studied amorphous alloy, heating up to 700 °C, which is after the exothermic peak in DTA, the samples are fully crystallized. Similar heat-treatment results were reported by Raanaei et al. [12,13,38] and Abbasi et al. [14]. Besides the formation of intermetallics, it also formed some undesirable

iron oxide phases, which was inadvertent, and it possibly have happened due to some unintentional presence of oxygen in the DTA cells. However, ferritic deposition during crystallization is known for FeCoNi based amorphous alloys, which are prone get rapid oxidation in the presence of oxygen.

3.4. Structure and stability of amorphous phase under high pressure by synchrotron XRD

Amorphous structure was characterized using experimentally obtained X-ray total structure factor, S(Q) and reduced total atomic pair distribution function, G(r). The S(Q) curve of ambient conditions (Figure 10a) was obtained from the experimental scattering intensity data collected from sample loaded in a 0.5 mm quartz capillary. The background intensity subtraction was performed using the pattern collected from empty capillary. The S(Q) data were then Fourier transformed to obtain reduced total atomic pair distribution function, G(r). The complete data reduction steps have been presented in Figure S1 in supplementary information.

The S(Q) curve is characterized by an intense primary peak at 3.09 $Å^{-1}$ indicating short range order at length scales of about 2.03 Å. There is a very good agreement between our S(Q) results and that of its counterparts amorphous Co-Ti [39] and Ni-Ti [22,28,40] alloys. This allowed us to discuss some other similarities in G(r). For instance, the shoulder on the right side of the second peak which is usually attributed to chemical short range order (CSRO) in amorphous structure [22] is clearly seen in at ~ 5.1 Å in Figure 10b despite our Q-range in S(Q) is limited to 7 $Å^{-1}$. Large oscillations below ~ 2.0 Å in G(r) indicate Fourier transform truncation caused by the finite range of Q measured. The atomistic origin of G(r), and direct understanding of the short and medium range structural aspects still remain unclear since it requires a study of a combination of state-of-the art high energy X-ray diffraction and 3D

Monte Carlo structural modeling. Stability of amorphous $(FeCoNi)_{70}Ti_{10}B_{20}$ has been tested in the pressure range of 0.1-30 GPa. The XRD patterns of amorphous $(FeCoNi)_{70}Ti_{10}B_{20}$ obtained during compression in the pressure range between ambient and 30 GPa are shown in Figure 10c. The results indicate that the amorphous phase is stable up to 30 GPa maximum pressure reached in this study. A shift of diffraction peaks to higher angles in 0.1-30 GPa pressure range simply indicates densification of amorphous phase.

3.5.Magnetic characterization

Magnetic field dependence of the magnetization (M(H)) of the as-milled powders and heat-treated samples (at 350 °C and 700 °C) measured at room temperature with an applied field -20 kOe < Hc < 20 kOe conditions are shown in Figure 11. For a better clarity, the inset in the Fig.11 shows the hysteresis loops at the region of low magnetic field (± 100 Oe). Results show that all powders exhibit typical soft ferromagnetic behavior. The saturation magnetization (Ms) of the as-milled samples of 1 h, 5 h and 50 h, and the 50 h milled sample annealed at 350 °C and 700 °C were determined as 95.8, 120.9, 107.2, 119.2, and 52.6 emu/g, respectively. Sample milled for 5 h exhibits the highest Ms value of 120.9 emu/g and further milling to 50 h results in a decrease in saturation magnetization. From Figure 2b it is evident that 5 h milled sample contains the α-Fe solid solution phase, and 50 h milled sample is amorphous phase of $(FeCoNi)_{70}Ti_{10}B_{20}$. The Ms of α-Fe nanoparticles was reported approximately 190 emu/g which explains the large saturation magnetization of the sample milled for 5 h [41]. After annealing the 50 h milled sample at 350 °C, the saturation magnetization significantly increases to 119.2 emu/g. This is probably owing to the enhancement of the ferromagnetic ordering with reduction in residual stress [13,16,38]. On the other hand, higher annealing temperature of 700 °C led to full crystallization of the sample and formation of intermetallics, iron oxide and unknown phases causing a pronounced

decrease in Ms. The coercivity (Hc) values of the as-milled samples for 1 h, 5 h and 50 h, and the 50 h milled sample annealed at 350 °C and 700 °C were determined as 31, 59, 33, 13 and 72 Oe, respectively. In general, coercivity is linearly dependent to magnetic anisotropy and demagnetization factor. In fine particles, it increases as particle size decreases and reaches a maximum value at single domain size [10]. However, in mechanically alloyed powders the coercivity is very sensitive to additional factors such as structural defects pinning the domain walls and internal strain. Thus, decrease of the Hc from 59 to 33 Oe as the milling time increases from 5 h to 50 h could be due to the combination of many effects. But it is clear that heat treatment of 50 h sample at 350 °C release the milling-induced internal stress and sample show good soft ferromagnetic behavior with low coercivity and high saturation magnetization.

4. Conclusions

The $(FeCoNi)_{70}Ti_{10}B_{20}$ (at%) alloy produced by mechanical alloying of elemental powders of Fe, Co, Ni, Ti and B was predominantly an amorphous alloy. Besides studying structural and morphological changes of the alloy by X-ray diffraction, scanning and transmission electron microscopy, the high-temperature and high-pressure studies were also performed to demonstrate the structural stability of the amorphous phase. The crystallite sizes of the alloy were sharply reduced as the milling progressed. However, such decrease was not noticeable beyond 20 h of milling. The crystallite size and lattice strain of 20 h milled powder alloy was estimated as 2.2 ± 1 nm and 4.3 %, respectively. The most interesting aspect of the present study is that the crystalline phases of the alloy were progressively reduced and amorphism of the alloy was increased with the milling time. The XRD analysis of 50 h milled sample confirmed complete disappearance of the crystalline phases. SEM images indicated nearly spherical shaped morphology of the amorphous alloy with a particle size of about 42 μm. The

elemental mapping and EDX analysis revealed complete homogeneity of the of elemental powders signifying perfect solid-solution of elements without any contaminations. DTA curves demonstrated that the crystallization of the amorphous phase of the 50 h milled sample commenced around 485 °C. Heat treatment of the powders above 485 °C resulted in the formation of the crystalline phases of the constituent elements. Therefore, the thermal stability of the amorphous phase cannot safely be ascertained above 485 °C. Whereas the amorphous phase of the alloy demonstrated remarkable high-pressure stability up to 30GPa confirmed by high-pressure synchrotron XRD studies. Heat-treatment of the 50 h milled amorphous powder at 350 °C enhanced softer magnetic behavior with higher Ms value (119.2 emu/g) and relatively lower Hc (13.4 Oe). This demonstrated the potential of the annealed amorphous $(FeCoNi)_{70}Ti_{10}B_{20}$ alloy as a functional magnetic material.

Acknowledgements

We would like to thank Zonguldak Bülent Ecevit University (Project no. 2015-73338635-01) for the financial support, Middle East Technical University for TEM measurements, Kastamonu University for VSM measurements, and Zonguldak Bülent Ecevit University, Science and Technology Application and Research Centre for the other characterization measurements. Beamline 12.2.2 at ALS is partially supported by COMPRES, the Consortium for Materials Properties Research in Earth Sciences under NSF Cooperative Agreement EAR 1606856. The Advanced Light Source is supported by the Director, Office of Science, Office of Basic Energy Sciences, of the U.S. Department of Energy under Contract No. DE-AC02-05CH11231.

References

[1] H. Shokrollahi, The magnetic and structural properties of the most important alloys of iron produced by mechanical alloying, Mater. Des. 30 (2009) 3374–3387. https://doi.org/10.1016/j.matdes.2009.03.035.

[2] A.H. Bahrami, H. Ghayour, S. Sharafi, Evolution of microstructural and magnetic properties of mechanically alloyed $Fe_{80-x}Ni_{20}Si_x$ nanostructured powders, Powder Technol. 249 (2013) 7–14. https://doi.org/10.1016/j.powtec.2013.07.024.

[3] D. Jiles, Introduction to Magnetism and Magnetic Materials, Springer US, Boston, MA, 1991. https://doi.org/10.1007/978-1-4615-3868-4.

[4] H.R. Lashgari, D. Chu, S. Xie, H. Sun, M. Ferry, S. Li, Composition dependence of the microstructure and soft magnetic properties of Fe-based amorphous/nanocrystalline alloys: A review study, J. Non. Cryst. Solids. 391 (2014) 61–82. https://doi.org/10.1016/j.jnoncrysol.2014.03.010.

[5] M.E. McHenry, M. a Willard, D.E. Laughlin, Amorphous and nanocrystalline materials for applications as soft magnets, Prog. Mater. Sci. 44 (1999) 291–433. https://doi.org/10.1016/S0079-6425(99)00002-X.

[6] A. Inoue, T. Zhang, H. Koshiba, A. Makino, New bulk amorphous Fe–(Co,Ni)–M–B (M=Zr,Hf,Nb,Ta,Mo,W) alloys with good soft magnetic properties, J. Appl. Phys. 83 (1998) 6326–6328. https://doi.org/10.1063/1.367811.

[7] C. Suryanarayana, Mechanical Alloying and Milling, Marcel Dekker Incorporated, 2004.

[8] M.S. El-Eskandarany, Mechanical Alloying: For Fabrication of Advanced Engineering Materials, Univ. Press of Mississippi, 2013.

[9] R. Koohkan, S. Sharafi, H. Shokrollahi, K. Janghorban, Preparation of nanocrystalline Fe-Ni powders by mechanical alloying used in soft magnetic composites, J. Magn.

Magn. Mater. 320 (2008) 1089–1094. https://doi.org/10.1016/j.jmmm.2007.10.033.

[10] G. Herzer, Grain size dependence of coercivity and permeability in nanocrystalline ferromagnets, IEEE Trans. Magn. (1990). https://doi.org/10.1109/20.104389.

[11] T. Şimşek, Investigation of the structural and magnetic properties of amorphous/nanocrystalline $Fe_{70}Ti_{10}B_{20}$ (%at.) alloys by mechanical alloying, J. Boron. 4 (2019) 85–91. https://doi.org/10.30728/boron.500470.

[12] H. Raanaei, V. Mohammad-Hosseini, Morphology and magnetic behavior of cobalt rich amorphous/nanocrystalline $(Co\text{-}Ni)_{70}Ti_{10}B_{20}$ alloyed powders, J. Magn. Magn. Mater. 414 (2016) 90–96. https://doi.org/10.1016/j.jmmm.2016.04.040.

[13] H. Raanaei, M. Rahimi, V. Mohammad-Hosseini, Nanostructured iron rich $(Fe\text{-}Co)_{70}$ $Mn_{10}Ti_{10}B_{10}$ mechanically alloyed powder: Synthesis and characterizations studies, J. Magn. Magn. Mater. 508 (2020) 166870. https://doi.org/10.1016/j.jmmm.2020.166870.

[14] S. Abbasi, H. Eslamizadeh, H. Raanaei, Study of synthesis, structural and magnetic properties of nanostructured $(Fe_{67}Ni_{33})_{70}Ti_{10}B_{20}$ alloy, J. Magn. Magn. Mater. 451 (2018) 780–786. https://doi.org/10.1016/j.jmmm.2017.12.015.

[15] S.W. Du, R.V. Ramanujan, Mechanical alloying of Fe–Ni based nanostructured magnetic materials, J. Magn. Magn. Mater. 292 (2005) 286–298. https://doi.org/10.1016/j.jmmm.2004.11.143.

[16] B. Avar, S. Ozcan, Characterization and amorphous phase formation of mechanically alloyed $Co_{60}Fe_5Ni_5Ti_{25}B_5$ powders, J. Alloys Compd. 650 (2015) 53–58. https://doi.org/10.1016/j.jallcom.2015.07.268.

[17] W.S. Rasband, ImageJ, Image Processing and Analysis in Java, National Institutes of Health, USA, 1.50V, (2014).

[18] B.X. Amelo, 'Pert HighScore Plus, version 3.0 e, The Netherlands. (2012).

[19] C. Prescher, V.B. Prakapenka, DIOPTAS : a program for reduction of two-dimensional

X-ray diffraction data and data exploration, High Press. Res. 35 (2015) 223–230. https://doi.org/10.1080/08957959.2015.1059835.

[20] A. Wederni, R. Lachheb, J.J. Suñol, J. Saurina, L. Escoda, M. Khitouni, Structural, microstructural and thermal properties of nanostructured $Fe_{60}Al_{35}Sn_5$ alloy synthesized by mechanical alloying, Mater. Charact. 148 (2019) 272–279. https://doi.org/10.1016/j.matchar.2019.01.001.

[21] R. Adelfar, H. Mirzadeh, A. Ataie, M. Malekan, Amorphization and mechano-crystallization of high-energy ball milled Fe-Ti alloys, J. Non. Cryst. Solids. 520 (2019) 119466. https://doi.org/10.1016/j.jnoncrysol.2019.119466.

[22] R.B. Schwarz, R.R. Petrich, C.K. Saw, The synthesis of amorphous NiTi alloy powders by mechanical alloying, J. Non. Cryst. Solids. 76 (1985) 281–302. https://doi.org/10.1016/0022-3093(85)90005-5.

[23] A. Inoue, Stabilization of metallic supercooled liquid and bulk amorphous alloys, Acta Mater. 48 (2000) 279–306. https://doi.org/10.1016/S1359-6454(99)00300-6.

[24] A. Takeuchi, A. Inoue, Classification of bulk metallic glasses by atomic size difference, heat of mixing and period of constituent elements and its application to characterization of the main alloying element, Mater. Trans. 46 (2005) 2817–2829. https://doi.org/10.2320/matertrans.46.2817.

[25] O.N. Senkov, D.B. Miracle, Effect of the atomic size distribution on glass forming ability of amorphous metallic alloys, Mater. Res. Bull. 36 (2001) 2183–2198. https://doi.org/10.1016/S0025-5408(01)00715-2.

[26] H. Minouei, G.H. Akbari, M.H. Enayati, S.I. Hong, Amorphization and nanocrystallization of Ni–Nb-Si Alloys, Mater. Sci. Eng. A. 682 (2017) 396–401. https://doi.org/10.1016/j.msea.2016.11.041.

[27] H. Dutta, A. Sen, J. Bhattacharjee, S.K. Pradhan, Preparation of ternary Ti0.9Ni0.1C

cermets by mechanical alloying: Microstructure characterization by Rietveld method and electron microscopy, J. Alloys Compd. 493 (2010) 666–671. https://doi.org/10.1016/j.jallcom.2009.12.184.

[28] E. Sakher, N. Loudjani, M. Benchiheub, M. Bououdina, Influence of Milling Time on Structural and Microstructural Parameters of $Ni_{50}Ti_{50}$ Prepared by Mechanical Alloying Using Rietveld Analysis, J. Nanomater. 2018 (2018) 1–11. https://doi.org/10.1155/2018/2560641.

[29] J.I. Langford, The accuracy of cell dimensions determined by Cohen's method of least squares and the systematic indexing of powder data, J. Appl. Crystallogr. 6 (1973) 190–196. https://doi.org/10.1107/s0021889873008460.

[30] H.W. Song, S.R. Guo, Z.Q. Hu, A coherent polycrystal model for the inverse Hall-Petch relation in nanocrystalline materials, Nanostructured Mater. 11 (1999) 203–210. https://doi.org/10.1016/S0965-9773(99)00033-1.

[31] J.M. Greneche, A. Ślawska-Waniewska, About the interfacial zone in nanocrystalline alloys, J. Magn. Magn. Mater. 215 (2000) 264–267. https://doi.org/10.1016/S0304-8853(00)00130-X.

[32] L. Karimi, H. Shokrollahi, Structural, microstructural and magnetic properties of amorphous/ nanocrystalline $Ni_{63}Fe_{13}Mo_4Nb_{20}$ powders prepared by mechanical alloying, J. Alloys Compd. 509 (2011) 6571–6577. https://doi.org/10.1016/j.jallcom.2011.03.060.

[33] A.N. Faruqui, P. Manikandan, T. Sato, Y. Mitsuno, K. Hokamoto, Mechanical milling and synthesis of Mg-SiC composites using underwater shock consolidation, Met. Mater. Int. 18 (2012) 157–163. https://doi.org/10.1007/s12540-012-0019-9.

[34] A.H. Taghvaei, A.M. Khoshrodi, Characterization, thermodynamic analysis and magnetic investigation of new soft magnetic amorphous/nanocrystalline

$Co_{50}Fe_{21}Ti_{19}Ta_5B_5$ powders produced by mechanical alloying, J. Alloys Compd. 742 (2018) 887–896. https://doi.org/10.1016/j.jallcom.2018.01.382.

[35] R. Amini, M.J. Hadianfard, E. Salahinejad, M. Marasi, T. Sritharan, Microstructural phase evaluation of high-nitrogen Fe-Cr-Mn alloy powders synthesized by the mechanical alloying process, J. Mater. Sci. 44 (2009) 136–148. https://doi.org/10.1007/s10853-008-3117-9.

[36] A.W. Weeber, H. Bakker, Amorphization by ball milling. A review, Phys. B Phys. Condens. Matter. 153 (1988) 93–135. https://doi.org/10.1016/0921-4526(88)90038-5.

[37] M.M. Verdian, M. Salehi, K. Raeissi, Synthesis of amorphous/nanocrystalline ni-ti powders by using low energy mechanical alloying, Int. J. Mod. Phys. B. 24 (2010) 1261–1269. https://doi.org/10.1142/S0217979210055251.

[38] H. Raanaei, H. Eskandari, V. Mohammad-Hosseini, Structural and magnetic properties of nanocrystalline Fe-Co-Ni alloy processed by mechanical alloying, J. Magn. Magn. Mater. 398 (2016) 190–195. https://doi.org/10.1016/j.jmmm.2015.09.031.

[39] K.D. Machado, D.F. Sanchez, J.C. de Lima, T.A. Grandi, Modeling the atomic structure of an amorphous $Co_{57}Ti_{43}$ alloy produced by mechanical alloying using RMC simulations, Solid State Commun. 148 (2008) 46–49. https://doi.org/10.1016/j.ssc.2008.07.027.

[40] T. Fukunaga, N. Watanabe, K. Suzuki, Experimental determination of partial structures in $Ni_{40}Ti_{60}$ glass, J. Non. Cryst. Solids. 61–62 (1984) 343–348. https://doi.org/10.1016/0022-3093(84)90572-6.

[41] J. Liu, K. Schliep, S. He, B. Ma, Y. Jing, D.J. Flannigan, J. Wang, Iron nanoparticles with tunable tetragonal structure and magnetic properties, Phys. Rev. Materials 2, (2018) 054415. https://doi.org/10.1103/PhysRevMaterials.2.054415.

Figures Captions

Figure 1 XRD pattern of initial powder mixture and corresponding phases.

Figure 2 (a) XRD patterns and (b) amorphous phase fraction of $(FeCoNi)_{70}Ti_{10}B_{20}$ alloys as a function of milling period.

Figure 3 (a) Crystallite size-lattice strain, (b) lattice parameters, (c) dislocation density and (d) volume fraction of grain boundaries of $(FeCoNi)_{70}Ti_{10}B_{20}$ alloys as a function of milling period.

Figure 4 Scanning electron microscope images of the powders milled at various milling period (a)1 h, (b) 3 h, (c) 5 h, (d)10 h, (e) 20 h, (f) 30 h, (g) 40 h and (h) 50 h.

Figure 5 Particle size distribution dependence to milling time.

Figure 6 Elemental mapping and EDX analysis of 50 h milled powders.

Figure 7 (a) Bright-field TEM images of 50h milled powders and (b) corresponding grain size distribution.

Figure 8 DTA plots of the milled powders for different milling periods.

Figure 9 XRD patterns of the 50 h milled powders heated up to 350 °C and 700 °C.

Figure 10 Total structure factor (a) and reduced total atomic pair distribution function, (b) of 50 h ball milled amorphous powders and (c) XRD patterns of mechanically alloyed amorphous sample collected in the pressure range of 0.1-30 GPa. Asteriks indicate Re gasket peaks.

Figure 11 M-H hysteresis curves of the as-milled powders and the heat-treated samples at 350 °C and 700 °C.

Table 1. Heats of mixing (ΔH_{mix}, kJ/mol) among the elements, and atomic radii of different elements used in the $(FeCoNi)_{70}Ti_{10}B_{20}$ alloy [24,25].

Element (atomic radius, nm)	Fe	Co	Ni	Ti	B
Fe (0.12412)	-	-1	-2	-17	-26
Co (0.12510)		-	0	-28	-24
Ni (0.12459)			-	-35	-24
Ti (0.14615)				-	-58
B (0.080200)					-

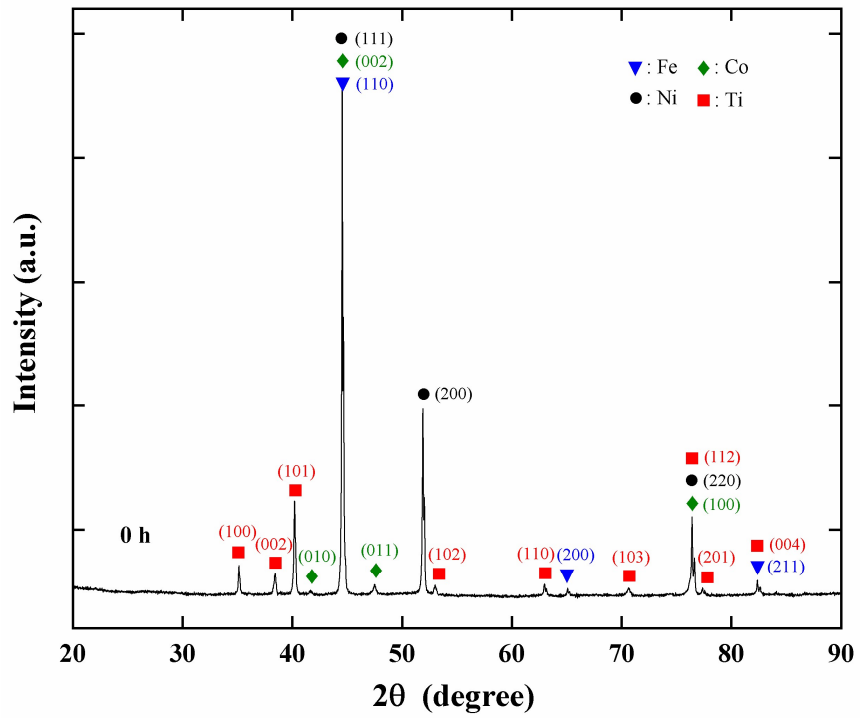

Figure 1. XRD pattern of initial powder mixture and corresponding phases.

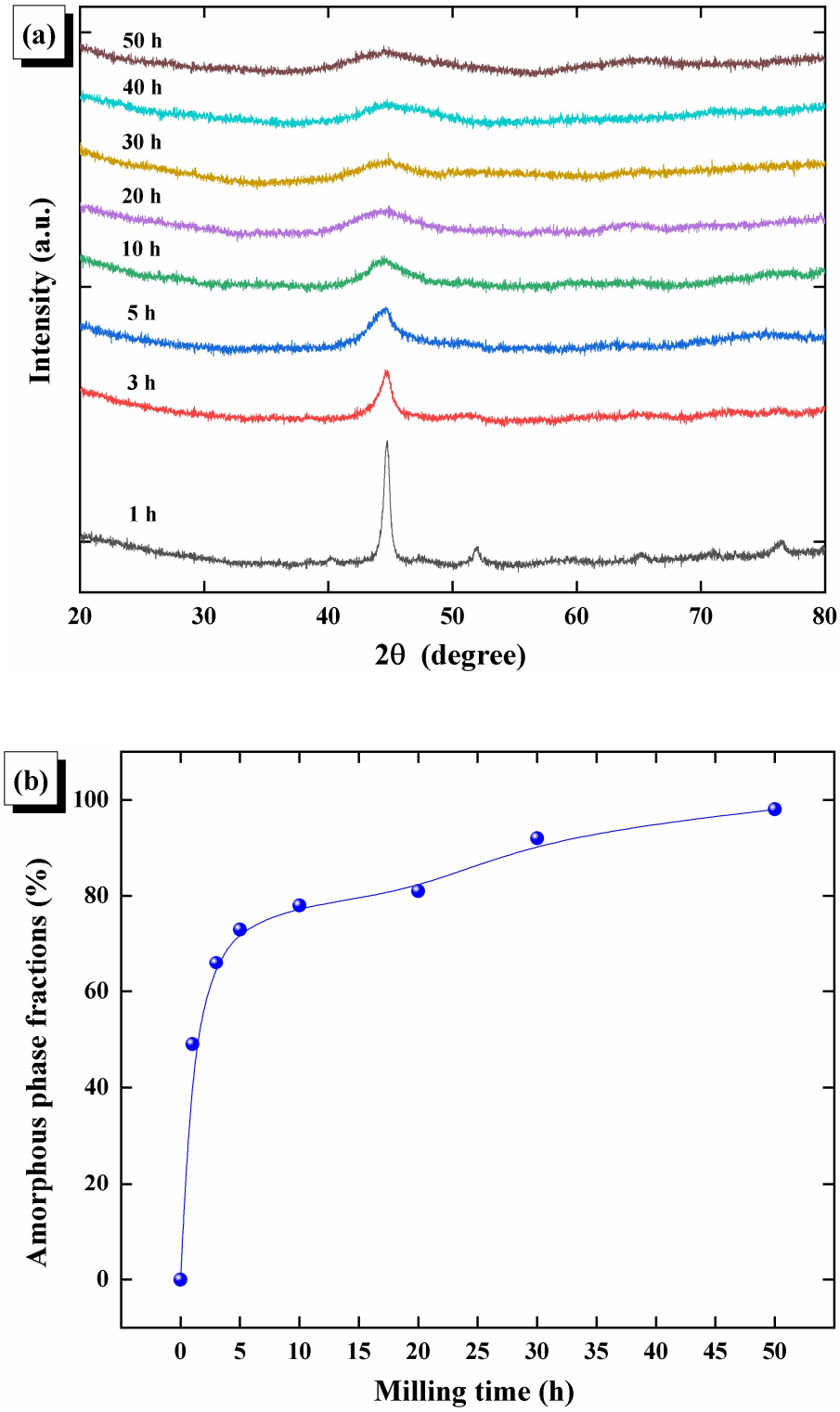

Figure 2. (a) XRD patterns and (b) amorphous phase fraction of $(FeCoNi)_{70}Ti_{10}B_{20}$ alloys as a function of milling period.

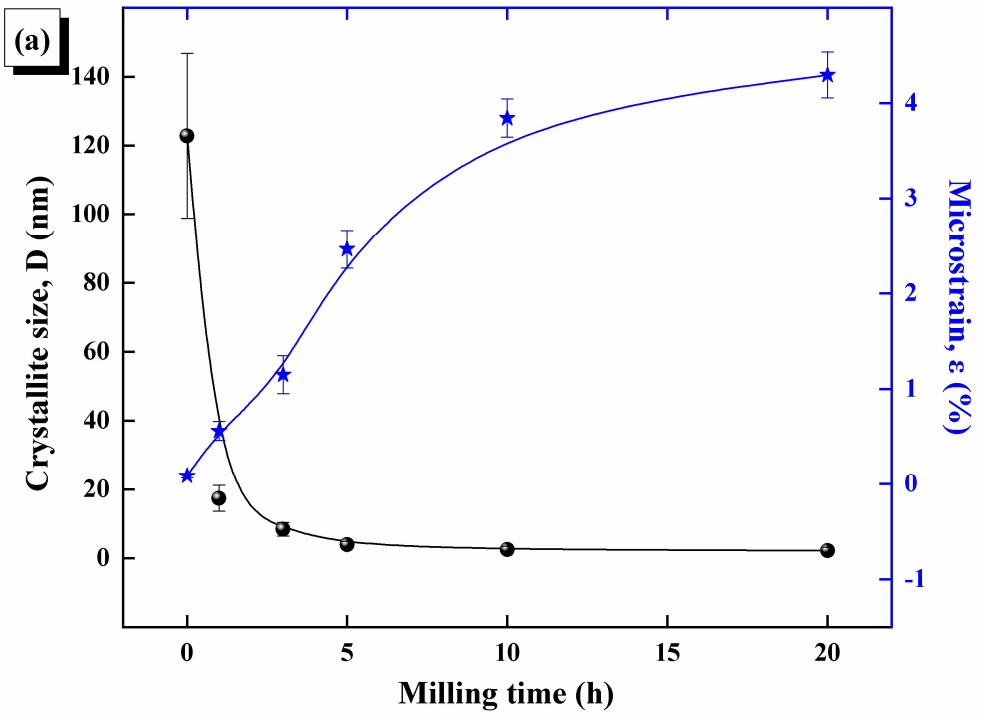
(a)
Crystallite size, D (nm)
Microstrain, ε (%)
Milling time (h)
0
20
40
60
80
100
120
140
-1
0
1
2
3
4
0
5
10
15
20

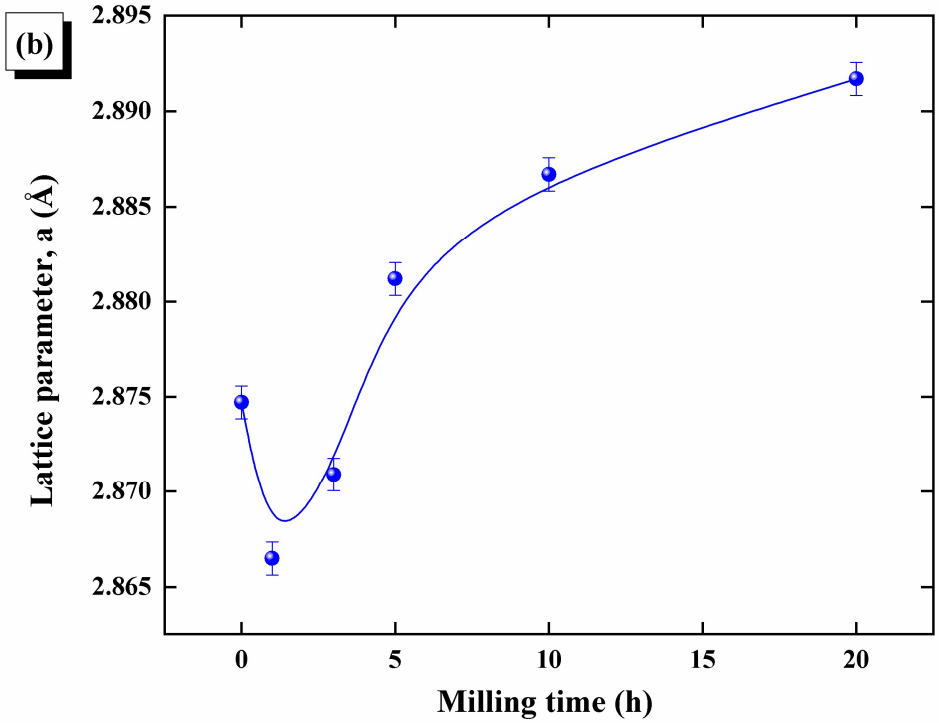
(b)
Lattice parameter, a (Å)
Milling time (h)
2.865
2.870
2.875
2.880
2.885
2.890
2.895
0
5
10
15
20

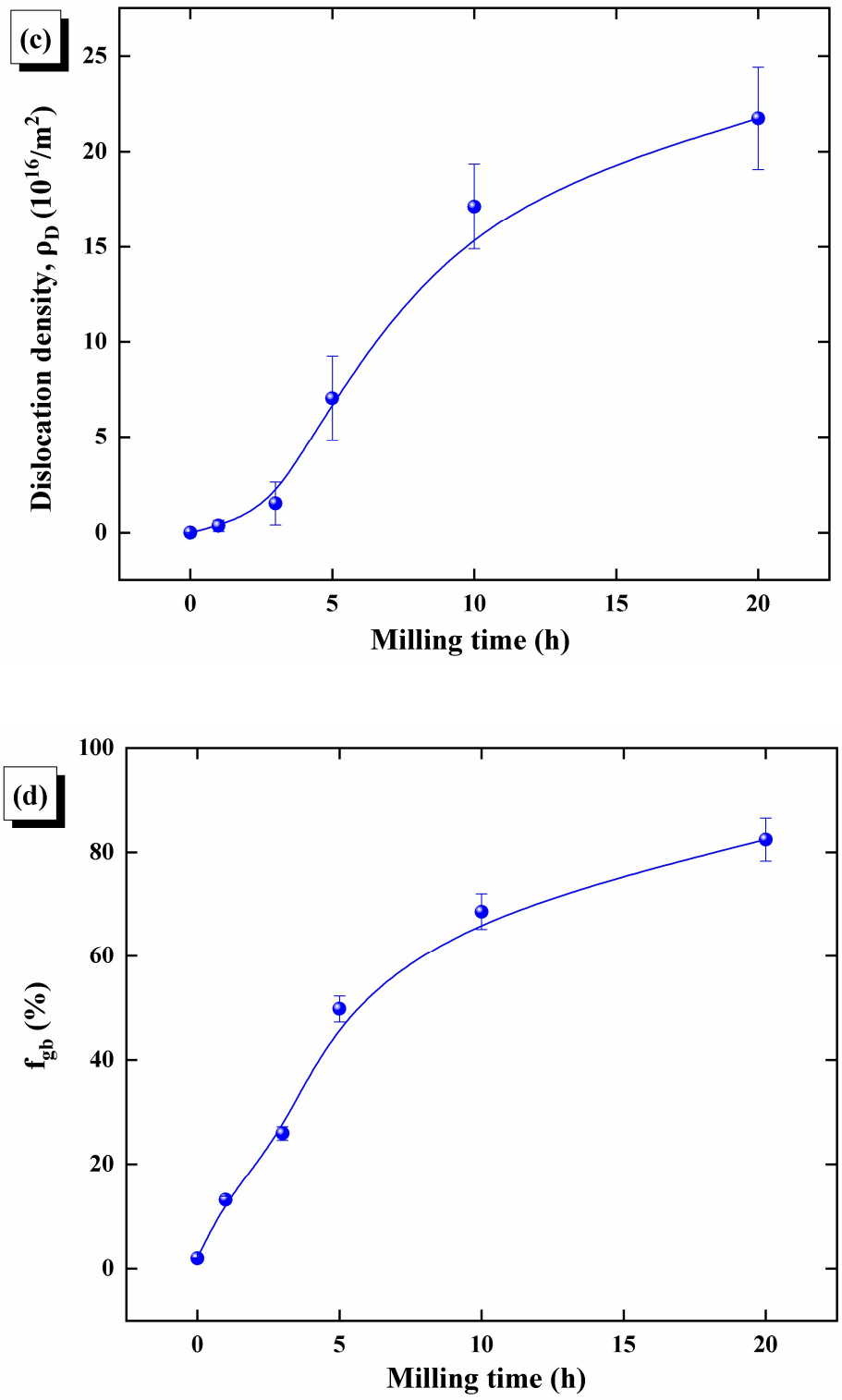

Figure 3. (a) Crystallite size-lattice strain, (b) lattice parameters, (c) dislocation density and (d) volume fraction of grain boundaries of $(FeCoNi)_{70}Ti_{10}B_{20}$ alloys as a function of milling period.

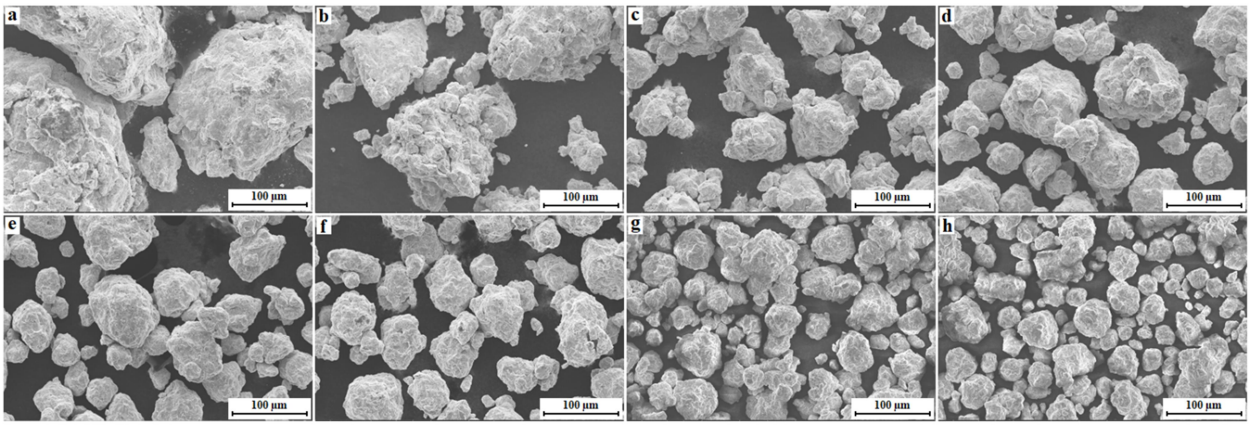

Figure 4. Scanning electron microscope images of the powders milled at various milling period (a)1 h, (b) 3 h, (c) 5 h, (d)10 h, (e) 20 h, (f) 30 h, (g) 40 h and (h) 50 h.

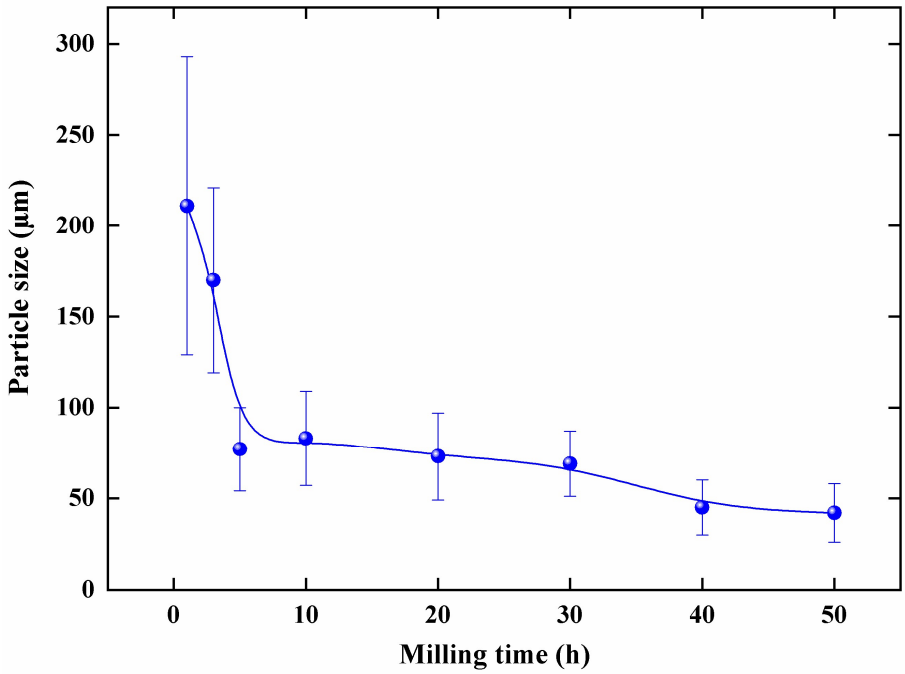

Figure 5. Particle size distribution dependence to milling time.

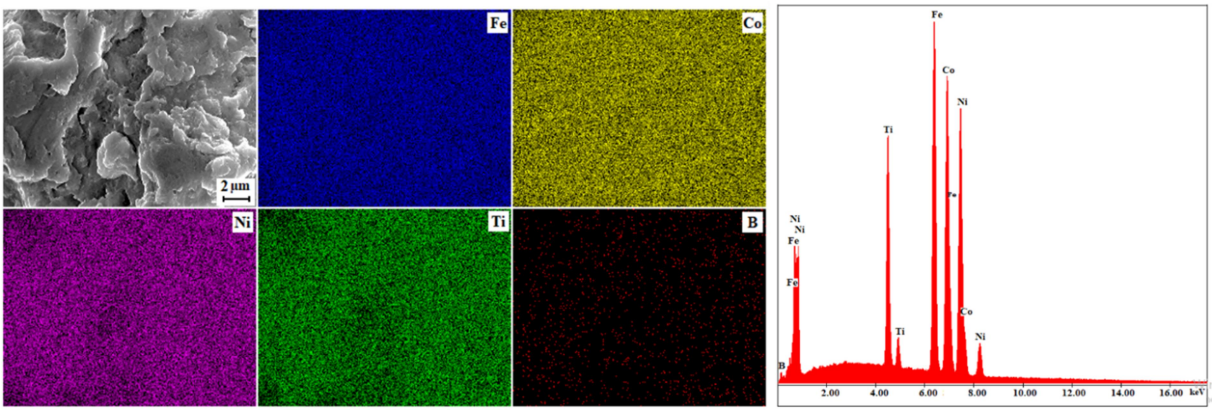

Figure 6. Elemental mapping and EDX analysis of 50 h milled powders.

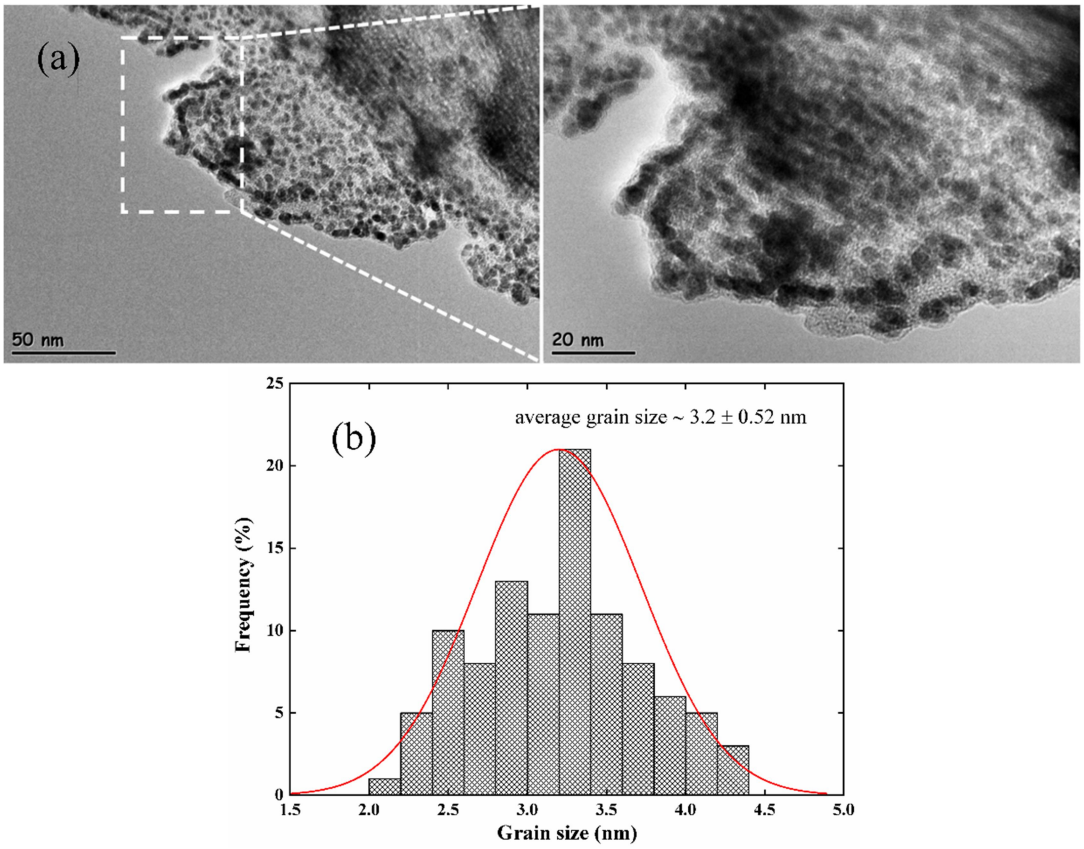

Figure 7. (a) Bright-field TEM images of 50h milled powders and (b) corresponding grain size distribution.

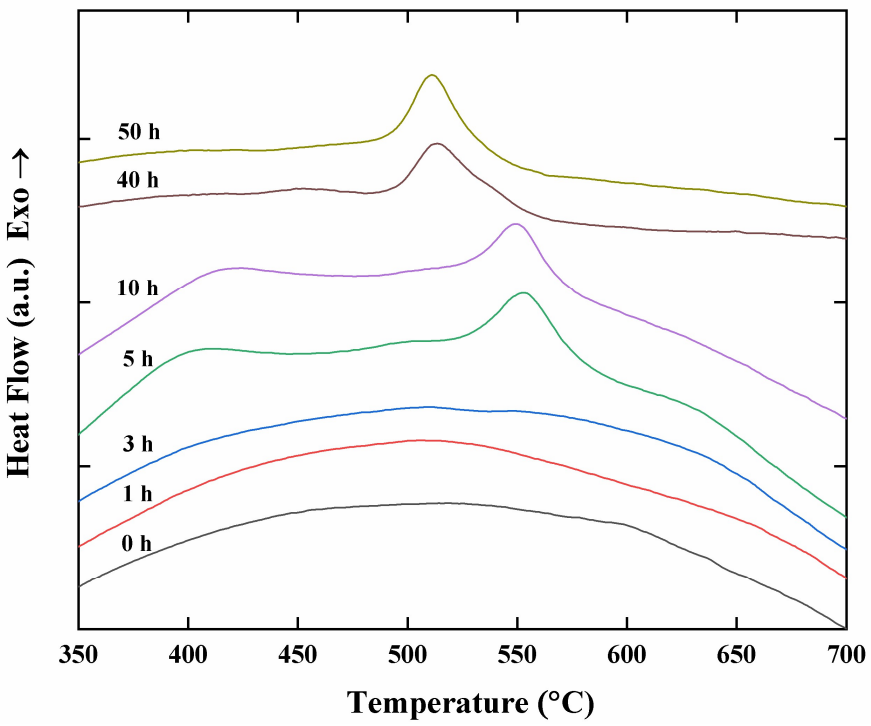

Figure 8. DTA plots of the milled powders for different milling periods.

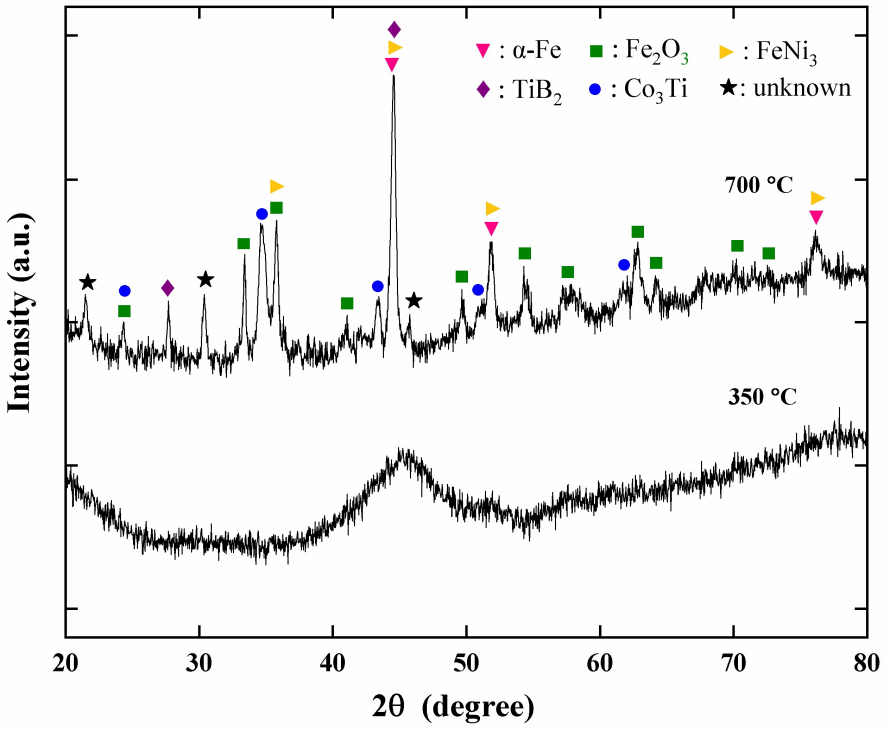

Figure 9. XRD patterns of the 50 h milled powders heated up to 350 °C and 700 °C.

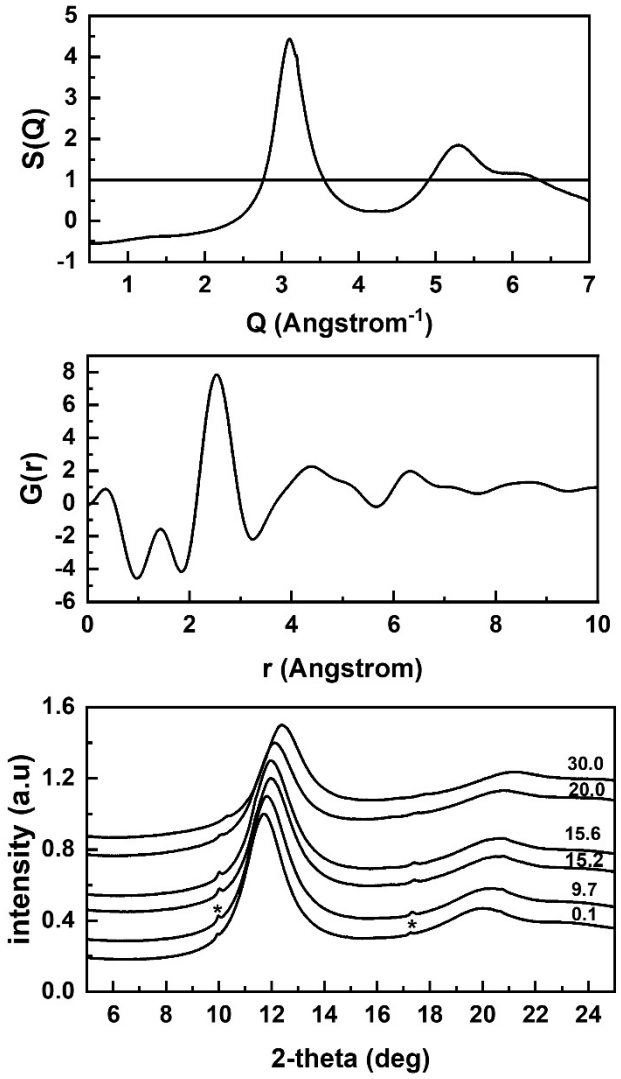

Figure 10. Total structure factor (a) and reduced total atomic pair distribution function, (b) of 50 h ball milled amorphous powders and (c) XRD patterns of mechanically alloyed amorphous sample collected in the pressure range of 0.1-30 GPa. Asteriks indicate Re gasket peaks.

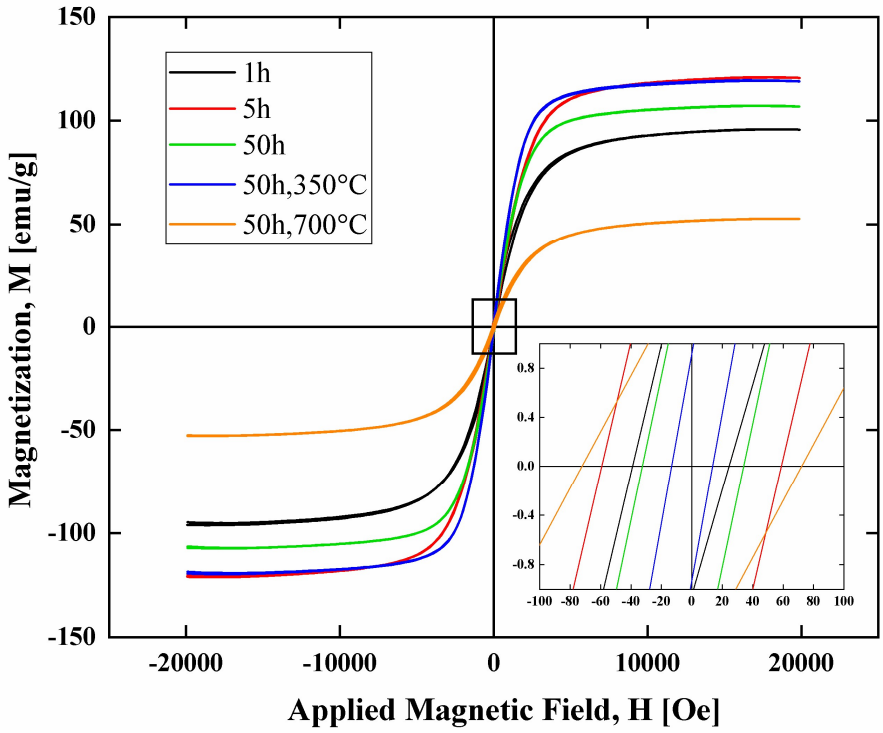

Figure 11. M-H hysteresis curves of the as-milled powders and the heat-treated samples at 350 °C and 700 °C.

Highlights

- Combination of nanocrystalline and amorphous phases during mechanical alloying of $(FeCoNi)_{70}Ti_{10}B_{20}$ powders.
- Average grain size of the final particles about 3.2 ± 0.52 nm by TEM images.
- Thermal stability of the amorphous phase formed after 50 h of milling of crystalline precursor up to 485 °C.
- Phase stability of the amorphous powders after 50 h of milling up to 30 GPa by high pressure synchrotron XRD studies.
- Obtaining a softer magnetic behavior after mechanical alloying followed by heat treatment process.

CRediT author statement

Baris Avar: Performed the experiments, Data analysis, Writing - Original Draft, Writing – Review & Editing, Supervision

Tuncay Sismsek: Performed the experiments, Data analysis, Writing - Original Draft

Sadan Ozcan: Supervision, Editing

Arun K. Chattopadhyay: Writing - Review & Editing

Bora Kalkan: Performed the high-pressure XRD experiments, Writing - Review & Editing